Systematic improvements in transmon qubit coherence enabled by niobium surface encapsulation

Check for updates

Mustafa Bal[1,15], Akshay A. Murthy [1,15], Shaojiang Zhu[1,15], Francesco Crisa[1,2,15], Xinyuan You[1], Ziwen Huang [1], Tanay Roy [1], Jaeyel Lee[1], David van Zanten[1], Roman Pilipenko [1], Ivan Nekrashevich[1], Andrei Lunin[1], Daniel Bafia [1], Yulia Krasnikova[1], Cameron J. Kopas [3], Ella O. Lachman[3], Duncan Miller[3], Josh Y. Mutus[3], Matthew J. Reagor [3], Hilal Cansizoglu[3], Jayss Marshall [3], David P. Pappas[3], Kim Vu[3], Kameshwar Yadavalli[3], Jin-Su Oh [4], Lin Zhou [4], Matthew J. Kramer [4], Florent Lecocq[5,6], Dominic P. Goronzy[7], Carlos G. Torres-Castanedo[7], P. Graham Pritchard[7], Vinayak P. Dravid [7,8,9], James M. Rondinelli [7], Michael J. Bedzyk [7,10], Mark C. Hersam [7,11,12], John Zasadzinski[2], Jens Koch [10,13], James A. Sauls [14], Alexander Romanenko [1] ✉ & Anna Grassellino[1] ✉

We present a transmon qubit fabrication technique that yields systematic improvements in T_1 relaxation times. We encapsulate the surface of niobium and prevent the formation of its lossy surface oxide. By maintaining the same superconducting metal and only varying the surface, this comparative investigation examining different capping materials, such as tantalum, aluminum, titanium nitride, and gold, as well as substrates across different qubit foundries demonstrates the detrimental impact that niobium oxides have on coherence times of superconducting qubits, compared to native oxides of tantalum, aluminum or titanium nitride. Our surface-encapsulated niobium qubit devices exhibit T_1 relaxation times 2–5 times longer than baseline qubit devices with native niobium oxides. When capping niobium with tantalum, we obtain median qubit lifetimes above 300 µs, with maximum values up to 600 µs. Our comparative structural and chemical analysis provides insight into why amorphous niobium oxides may induce higher losses compared to other amorphous oxides.

With massive improvements in device coherence times and gate fidelity over the past two decades, superconducting qubits have emerged as a leading technology platform for quantum computing[1–3]. Although many of these improvements have been driven through optimized device designs and geometries, the presence of defects and impurities at the interfaces and surfaces in the constituent materials continues to limit performance and serve as a critical barrier in achieving scalable quantum systems[4–6].

Specifically, these uncontrolled defect sites can serve as sources of loss by introducing two-level systems (TLS) or nonequilibrium quasiparticles[7–10]. As a result, researchers have recently begun to take a materials-oriented approach to understand and eliminate these sources of quantum decoherence in superconducting qubit devices.

Niobium (Nb) has been widely employed as the primary material in superconducting qubits as it possesses the largest critical temperature and

[1]Superconducting Quantum Materials and Systems Division, Fermi National Accelerator Laboratory (FNAL), Batavia, IL 60510, USA. [2]Department of Physics, Illinois Institute of Technology, Chicago, IL 60616, USA. [3]Rigetti Computing, Berkeley, CA 94710, USA. [4]Ames Laboratory, U.S. Department of Energy, Ames, IA 50011, USA. [5]National Institute of Standards and Technology, Boulder, CO 80305, USA. [6]Department of Electrical, Computer & Energy Engineering, University of Colorado, Boulder, CO 80309, USA. [7]Department of Materials Science and Engineering, Northwestern University, Evanston, IL 60208, USA. [8]The NUANCE Center, Northwestern University, Evanston, IL 60208, USA. [9]International Institute of Nanotechnology, Northwestern University, Evanston, IL 60208, USA. [10]Department of Physics and Astronomy, Northwestern University, Evanston, IL 60208, USA. [11]Department of Chemistry, Northwestern University, Evanston, IL 60208, USA. [12]Department of Electrical and Computer Engineering, Northwestern University, Evanston, IL 60208, USA. [13]Center for Applied Physics and Superconducting Technologies, Northwestern University, Evanston, IL 60208, USA. [14]Hearne Institute of Theoretical Physics, Department of Physics and Astronomy, Louisiana State University, Baton Rouge, LA 70803, USA. [15]These authors contributed equally: Mustafa Bal, Akshay A. Murthy, Shaojiang Zhu, Francesco Crisa.
✉e-mail: aroman@fnal.gov; annag@fnal.gov

superconducting gap of elemental superconductors, making thermal quasiparticle contribution to losses negligible at typical operating temperatures of on the order of tens of mK. It is also highly compatible with industrial-scale processes[11]. Furthermore, the Fermilab superconducting radio-frequency (SRF) research group has demonstrated in prior detailed studies of 3D cavities in the quantum regime that devices processed from Nb can sustain photon lifetimes as high as 2 s when the surface niobium oxide hosting sources of TLS is removed[12]. This is ~3 orders of magnitude longer than coherence times reported in the highest-performing transmon qubits[13,14], making bare niobium metal an attractive base material for further improvements in 2D superconducting qubits.

These previous measurements have unambiguously identified the surface oxide that forms spontaneously on Nb under ambient conditions as the major source of microwave loss[12,15–20]. Through 3D cavity measurements, we find that the loss tangent of this 5 nm thick oxide is ~0.1, which is orders of magnitude larger than the losses at the metal/substrate interface as well as those in the underlying substrate[21,22]. As a result, the removal of this oxide has been shown to boost the photon lifetime by 50–200× in 3D Nb SRF cavities in the TLS-dominated, <1 K regime. Other studies on 2D devices have since further confirmed the detrimental effect of this oxide[23,24].

Several recent studies have sought to mitigate losses associated with this region. Unfortunately, most methods for avoiding these losses are incompatible with integration into complex or large-scale manufacturing process flows. In one of the successful approaches, the surface oxide was removed by annealing the sample at temperatures at or exceeding 300 °C[12], with an almost complete elimination of the TLS-induced losses. While this thermal dissolution method is effective, sustained vacuum is required afterwards to prevent the regrowth of the surface oxide when the cavity or qubit is removed from an ultra-high vacuum (UHV) environment. An alternative oxide removal method involving HF as a wet etchant has been explored as well[23,24]. This process cannot be performed in vacuum, leading to rapid oxide regrowth afterwards. Furthermore, it can lead to hydrogen incorporation in the underlying niobium which can introduce resistive niobium hydrides[25–27]. Finally, nitrogen plasma passivation techniques have been identified as effective methods to partially suppress oxide formation[28,29].

Here, we propose a new strategy based on surface encapsulation to eliminate and prevent the formation of this lossy Nb surface oxide upon exposure to air. The first method involves depositing in situ metal capping layers of Al and Ta onto the Nb films in UHV. The second method involves atomic layer deposition to reduce the native Nb surface oxide by reacting it with a precursor and then depositing a thin metal film (TiN) that exhibits a reduced microwave loss. The third method involves milling away the oxide with Ar^+ ions and depositing a thin metal layer of Au with e-beam evaporation. Based on our systematic study, we observe that each of these surface passivation strategies effectively eliminate Nb_2O_5 and yield a clear improvement in coherence times. Of these capping approaches, we find that the Ta-capped Nb films exhibit the largest improvement and lead to devices with median relaxation times of 300 μs. Finally, we explore the scalability of such an approach by repeating the fabrication of test devices with the Ta capping strategy at a commercial qubit fabrication and measurement facility and are able to replicate the results on Si substrates.

Results and discussion
Qubit fabrication
We fabricated seven sets of qubits for this study as outlined in Table 1 with device geometries provided in Fig. 1a. In terms of surface participation ratio, this is largest for device geometry A, followed by device geometry C, and smallest for device geometry B. Details of the fabrication procedure are provided in the Supplementary Information. Results from structural and chemical analysis of the fabricated qubits are provided in Figs. 1b and 2.

Table 1 | List of fabricated transmon qubits

Substrate	Film	Surface Encapsulation	Foundry	Measurement Site
Sapphire	Nb	-	PNF	Fermilab
Sapphire	Nb	Ta (Sputtering)	PNF	Fermilab
Sapphire	Nb	Al (Sputtering)	PNF	Fermilab
Sapphire	Nb	TiN (ALD)	PNF	Fermilab
Sapphire	Nb	Au (Evaporation)	PNF	Fermilab
Silicon	Nb	-	Rigetti	Rigetti
Silicon	Nb	Ta (Sputtering)	Rigetti	Rigetti

Figure 1b shows a low-magnification scanning transmission electron microscopy (STEM) image of a cross-section taken from a superconducting circuit. The superconducting metal (Nb) and metal capping layer (Ta) are labeled. Chemical phase maps generated using STEM energy dispersive spectroscopy are presented in Fig. 2a–d for the Nb films capped with different layers. We find that the capping layers are between 5 and 10 nm thick, as targeted. Additionally, the layers are spatially distinct with minimal intermixing present.

In order to assess the efficacy of the capping layers in preventing Nb_2O_5 formation, we analyze each film with time-of-flight secondary ion mass spectrometry (ToF-SIMS). This technique combines high mass resolution and sensitivity to both light and heavy elements with <100 nm spatial resolution, and has been employed extensively to identify impurities such as oxides in superconducting qubits[16,30]. As ToF-SIMS enables the identification of different oxide species based on their mass to charge (M/Z) ratios, we are able to resolve that the surface oxide is primarily composed of Nb_2O_5 based on the presence of localized signal corresponding to the presence of $Nb_2O_5^-$ ions in this region.

To better understand how this oxide is impacted by metal capping, we compare the $Nb_2O_5^-$ signal counts measured from the surface of the baseline Nb sample to the $Nb_2O_5^-$ signal counts measured at the interface between the capping layer and the Nb metal in the capped Nb samples as indicated in Fig. 2e. We note that this does not refer to total oxide quantity (as aluminum and tantalum themselves oxidize), but specifically to the reduction of the loss channel of particular interest, Nb_2O_5. The methodology is described in Supplementary Fig. 1 and the results are presented in Fig. 2e. We find that all of the capping strategies are highly effective in mitigating Nb_2O_5 formation. The Ta capping is particularly effective as a 1000× decrease in measured $Nb_2O_5^-$ is observed with this strategy. The results also suggest that in situ sputter deposition may be slightly more effective at protecting against surface oxidation compared to the other two methods. Finally, we observe the presence of a sharp interface between the Nb film and the underlying sapphire as shown in Fig. 2f. In contrast to Nb films grown on silicon where alloyed regions on the order of 5 nm have been observed, in Nb/sapphire structures we observe minimal intermixing present at the metal/substrate interface[31].
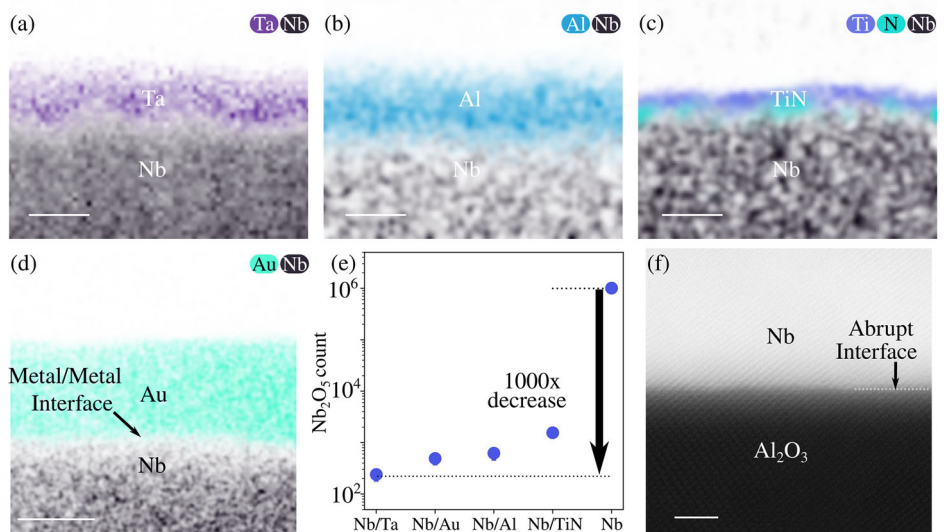
Qubit results
To most easily observe the impact of the metal capping layer on the superconducting qubit coherence, we performed measurements using the qubit geometry with the largest surface participation ratio (geometry A). These measurements were performed on the capped devices and on baseline Nb devices that were not capped.

The qubit devices are measured inside a dilution refrigerator at a temperature of around 40 mK via dispersive readout. The cryogenic wiring diagram is shown in Fig. 1c. Both qubit and readout pulses are sent through a single RF line. At the mixing chamber plate, two six-pole-single-throw microwave switches are used to direct the signals to the relevant sample and to extract the outgoing signal. After initial qubit spectroscopy, a Rabi measurement (Fig. 1d) is performed to determine the π-pulse length followed by T_1 measurements (Fig. 1e).
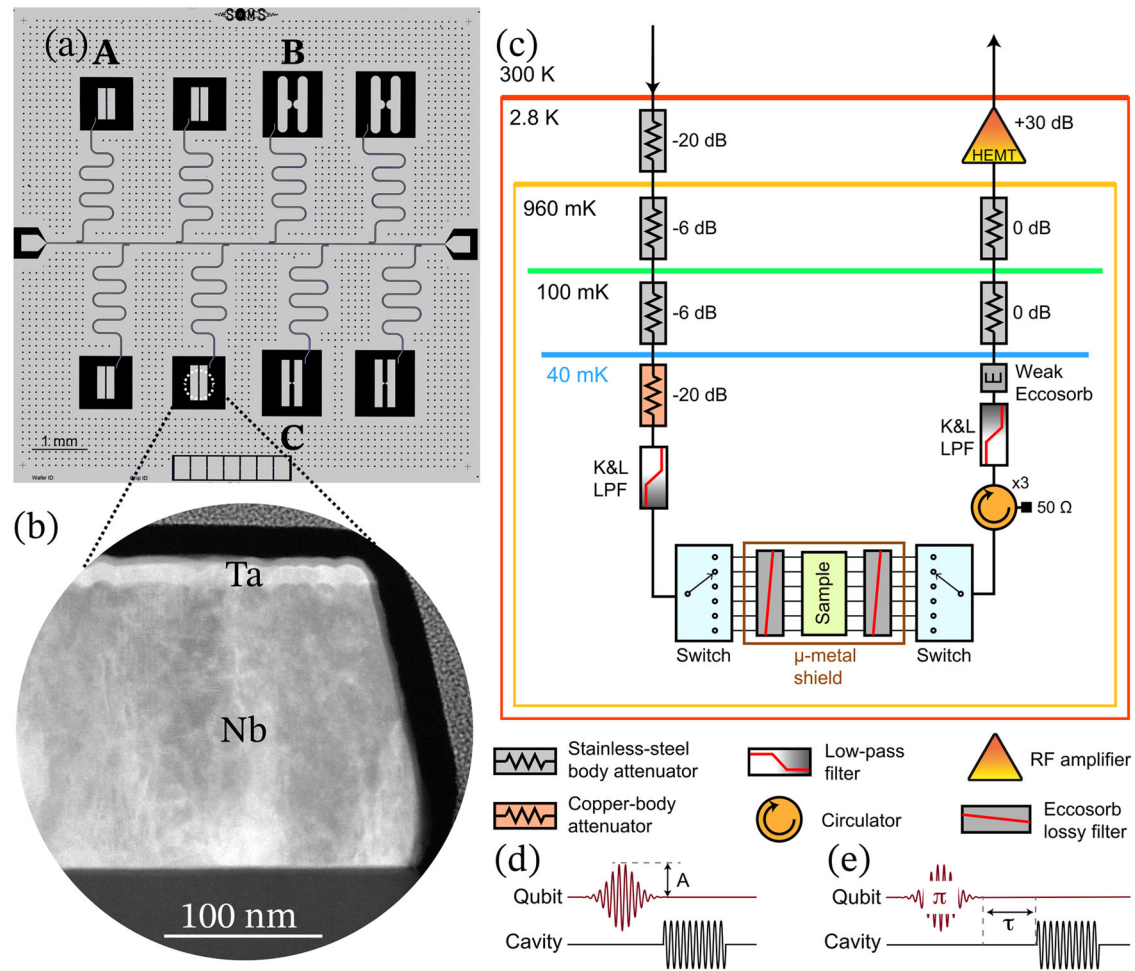
Fig. 1 | Qubit geometry and measurement setup. a 8 qubit chip layout consisting of three different geometries. **b** Low magnification annular dark field scanning transmission electron microscopy (ADF-STEM) image taken from a cross-section of a Nb transmon qubit where the Nb film is capped with a Ta metal layer. **c** Cryogenic wiring diagram. **d, e** Pulse scheme for characterization and plots. **d** Pulse for Rabi experiment used to calibrate π pulses. **e** Pulse for T_1 experiment.

Fig. 2 | Structural and chemical characterization of transmon qubit. a–d Chemical phase maps generated through STEM energy dispersive spectroscopy of the Nb films capped with Ta, Al, TiN, and Au, respectively. The Ta, Al, and Au capping layers are roughly 10 nm thick and the TiN layer is roughly 5 nm thick. **e** Plot depicting Nb_2O_5 counts captured with ToF-SIMS. Each of the capping strategies is effective in mitigating Nb_2O_5 formation. The Ta capping is particularly effective as a $1000\times$ decrease in $Nb_2O_5^-$ counts is observed with this strategy. **f** ADF-STEM image of the metal/substrate interface. Minimal intermixing is observed between Nb and the underlying c-plane sapphire substrate. Scale bars in (**a**)–(**d**) represent 10 nm. Scale bar in (**f**) represents 2 nm.
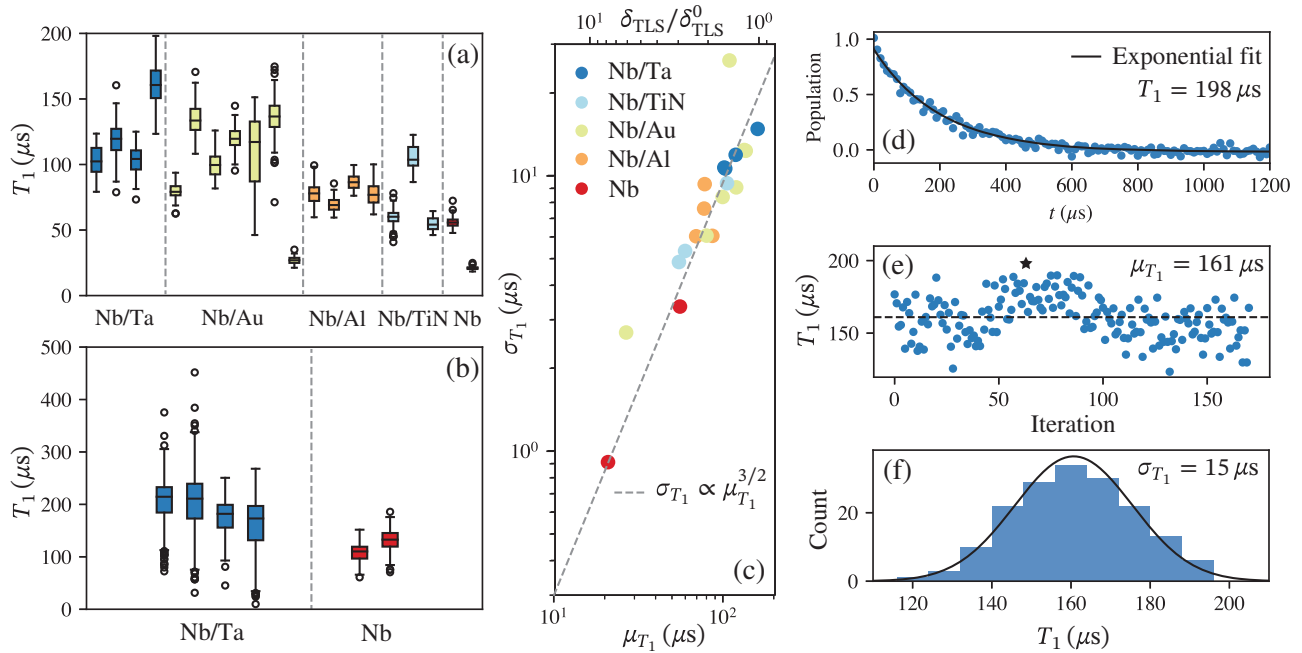
Fig. 3 | Qubit measurement results. a T_1 comparison of the five sets of qubit devices that were prepared on sapphire substrates. All four Nb/Ta qubits on the chip show $T_1 > 100$ μs, and the largest T_1 measured for Nb control qubits is ~50 μs. Boxes mark the 25th percentile and the 75th percentile of the measurement distribution over the course of 10 h of consecutive measurements. The line inside each box represents the median value. Error bars represent 95% confidence interval and circles represent outliers. **b** Measured T_1 values for test devices fabricated on silicon substrates. We observe a clear improvement in terms of the median T_1 value following surface capping of Nb with Ta. **c** Dependence of T_1 standard deviation, σ_{T1}, on the average

T_1, μ_{T1}. Different colors correspond to the different encapsulation groups shown in (**a**). Dashed line shows the best fitting of $\sigma_{T_1} \propto \mu_{T_1}^{3/2}$, according to ref. 36. It also shows that the Nb/Ta qubit has 5–10 times improvement of TLS loss compared with the Nb qubit, after converting the number of TLS into the tangent loss, δ_{TLS}. **d** Best $T_1 = 198$ μs. **e** Statistics for T_1 consecutively measured over 10 h, the average T_1 (μ_{T1}) is 161 μs and the standard deviation (σ_{T1}) is 15 μs. The star shows the iteration that yielded the best T_1 (see (**d**) for the decay curve). **f** Histogram of the T_1 values in (**e**), with a Gaussian fit.

Because the qubit energy relaxation time, T_1, is largely dependent on the material losses in the qubit device, while the dephasing time, T_2, is heavily impacted by many environmental factors such as the thermal noise, IR radiation, and cosmic rays[32,33], we focus on qubit T_1 characterization. The qubit T_1 characterization is widely believed to directly reflect the loss due to TLS, which is the focus of this work. The measurement follows the standard procedure[34], i.e., the qubit is driven from the ground to the first-excited state by a calibrated π pulse. The qubit state is then read after a variable delay. The measured signal decay is fitted exponentially to extract the qubit relaxation time, T_1. In order to probe both the typical and exceptional T_1 times, we benchmark the T_1 measurement by continuously collecting data for several hours for each qubit, as described in ref. 4. Using this data set, we extract the average, standard deviation, and best T_1 values, which we compare across different devices.

A comparison of the T_1 measured for different devices is provided in Fig. 3a and further summarized in Supplementary Table 1. The Nb qubits capped with Ta as well as the Nb qubits capped with Au have the highest average T_1 (>100 μs), while the baseline Nb qubits have the lowest average T_1. The average T_1 value of Nb qubits capped with Al is slightly higher than that of Nb qubits capped with TiN. The improvement in average T_1 for all of the capped devices suggests that reducing the native Nb_2O_5 (a strong TLS host) on the surface of the Nb film improves qubit energy relaxation times. Whiskers or circles in the plot indicate the maximum and minimum T_1 values observed during measurement windows on the order of a few hours per qubit [see Fig. 3d for the best T_1 decay curve]. The fluctuations of T_1 over time [shown in Fig. 3e], and its Gaussian distribution [shown in Fig. 3f] have both been observed in literature[4,35], and are presumably considered a signature of qubit lifetime limited by TLS defects residing in the materials.

To quantitatively compare TLS densities from different encapsulations, we calculate the average (μ_{T1}) vs. standard deviation (σ_{T1}) T_1 for each of the qubits that were measured continuously for 10 hours.

According to TLS theory[36], μ_{T1} and σ_{T1} can be represented by the following relations:

$$\mu_{T_1} = \alpha/(\omega N), \tag{1}$$

$$\sigma_{T_1} = \beta/(\omega N)^{3/2}, \tag{2}$$

where α and β are temperature-dependent constants and ω is the qubit frequency, which is treated as constant in this case as the qubit frequencies all lie within the range of 4 to 6 GHz. N is proportional to the number of TLS present in the qubit. From Eqs. (1) and (2), we find that $\sigma_{T_1} \propto \mu_{T_1}^{3/2}$ and the data is in agreement with this relationship (dashed line in Fig. 3c). Based on this plot, we determine that Nb qubits capped with Ta and Nb qubits capped with Au exhibit the smallest number of TLS and the highest μ_{T1}, maximum T_1 and fluctuations σ_{T1}. Conversely, the baseline Nb qubit exhibits the greatest number of TLS and therefore the lowest average T_1. Assuming TLS loss tangent, δ_{TLS}, is proportional to the number of TLS[9], we plot the relative change of δ_{TLS} for each set of devices, as shown in Fig. 3c. We find 5–8× reduction in loss between the Ta-capped Nb devices and the baseline Nb devices. Additionally, we find that the loss associated with Al-capped Nb qubits is slightly lower than TiN-capped Nb qubits. These results are also in agreement with the qubit T_1 measurements.

To assess the reproducibility, scalability and applicability of this capping method to other substrates, Ta-capped and Nb-only devices (with the same test geometry) were fabricated in the Rigetti Computing quantum integrated circuit foundry (Fremont, California) on high-resistivity Si(100) substrates. More details of this fabrication process can be found in ref. 6. The Ta-capped devices exhibit a systematic improvement in median T_1 (~200 μs) compared to the baseline Nb qubits (~120 μs). A box plot providing information on the measurements performed on both sets of qubits is provided in Fig. 3b with a maximum measured T_1 value of 451 μs. The consistent improvement in median T_1 for the capped Nb devices for both
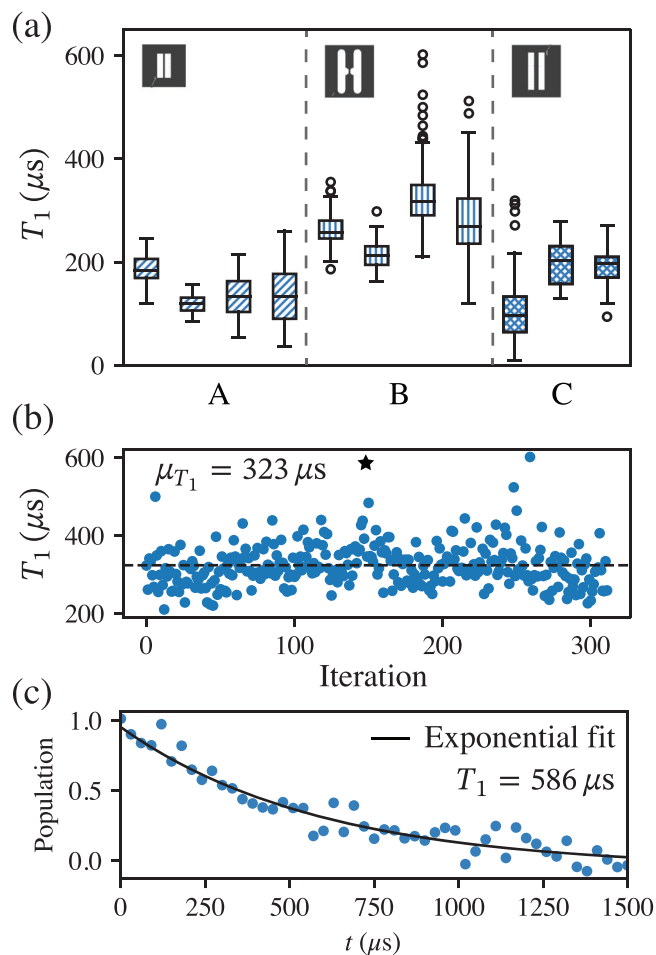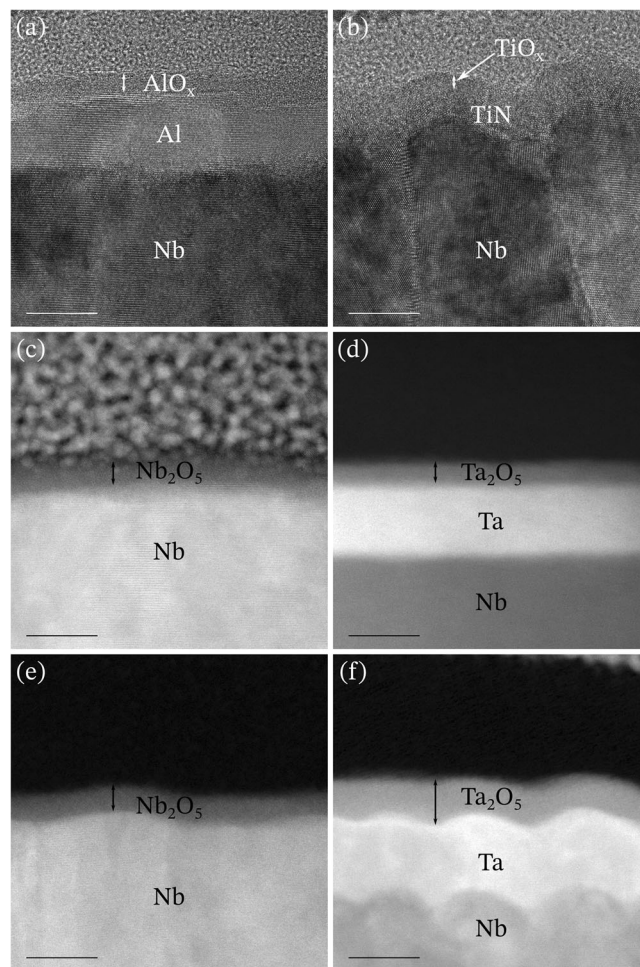
Fig. 4 | Effect of qubit geometry. a T_1 comparison of Nb/Ta qubits as a function of three different qubit geometries prepared on sapphire substrates. Geometry B yields the largest T_1 values. Error bars represent 95% confidence interval. **b** Statistics for T_1 consecutively measured over 70 h for a Geometry B qubit. The average T_1 (μ_{T_1}) is 323 μs. **c** Decay curve associated with measured T_1 value of 586 μs (indicated by star in (**b**)).

Fig. 5 | Electron microscopy images of surface oxides observed. Oxides for (**a**) Al-capped Nb, (**b**) TiN-capped Nb, (**c**) baseline Nb, and (**d**) Ta-capped Nb qubits prepared on sapphire are presented. Similar images of surface oxides for (**e**) baseline Nb, and (**f**) Ta capped Nb qubits prepared on silicon are also presented. The oxides are identified with arrows and tabulated in Table 2. Scale bars represent 10 nm.

silicon and sapphire substrates supports a performance limitation imposed by the amorphous Nb_2O_5 surface oxide in un-capped devices. Meanwhile, the T_2, $T_{2\ echo}$, and T_ϕ values are provided in Supplementary Fig. 2. The T_2, $T_{2\ echo}$, and T_ϕ values also increase following capping of Nb with Ta, although the spread in values is larger, as expected given their dependencies on additional extrinsic factors.

Given these promising T_1 results, we also fabricated larger footprint qubit geometries of the Ta-capped Nb (Geometry B and C) on sapphire that are comparable to those used by groups that have demonstrated the largest T_1 values to date[13,14]. In Fig. 4, a comparison of the measured T_1 values for a Ta-capped device is provided for the three different geometries that were investigated. These results are also summarized in Supplementary Table 2. Geometry B yields T_1 values with median qubit relaxation times above 300 μs, which are in line with the median qubit relaxation times reported by these groups. Further, we observe several individual measurements in excess of 550 μs over the course of several days. These are the leading values published to date for transmon qubits. These results, combined with the fact that this approach is reliable with both silicon and sapphire substrates and can be performed at room temperature makes surface encapsulation a very attractive methodology for achieving high coherence qubits. Moreover, future studies will involve gold encapsulation and other similar low-loss capping layers with similar larger footprint geometries to potentially push the envelope of performance even further.

Together, these results clearly demonstrate that eliminating Nb_2O_5 enhances the T_1 relaxation time of Nb transmon qubits. In the case of

Table 2 | Surface oxides observed on fabricated transmon qubits

Substrate	Film	Surface Encapsulation	Surface Oxide	Thickness	Average T_1 (μs)
Sapphire	Nb	-	Nb_2O_5	3–5 nm	40
Sapphire	Nb	Ta	Ta_2O_5	3–5 nm	120
Sapphire	Nb	Al	AlO_x	2–4 nm	75
Sapphire	Nb	TiN	TiO_x	1–2 nm	72
Sapphire	Nb	Au	Not Observed	-	114
Silicon	Nb	-	Nb_2O_5	1–2 nm	110
Silicon	Nb	Ta	Ta_2O_5	5–7 nm	200

devices capped with Ta, Al, and TiN, we still observe the presence of amorphous oxides of a few nm thickness such as Ta_2O_5, AlO_x, and TiO_x, respectively at the sample surface (Figs. 5 and S3). By linking modifications solely to the metal/air interface to measured T_1 values, we observe a trend where Ta_2O_5 ranks as the least lossy oxide of those measured, followed by Al_2O_3, TiO_2, and finally, Nb_2O_5. Further, the loss introduced by these various surface oxides does not appear to be directly correlated to their individual thicknesses as illustrated in Table 2. In particular, 1–2 nm TiO_x at

Fig. 6 | Nanoscale chemical analysis of Ta oxide.
a Darkfield STEM image of the Ta_2O_5/Ta interface.
Electron energy loss spectra (EELS) taken from the
locations indicated in (**a**) are provided in (**b**) and (**c**).
b EELS signal taken from the specified region
demonstrating how the tantalum $O_{2,3}$ edge evolves
with position. **c** EELS signal taken from the specified
region demonstrating how oxygen K edge evolves as
a function of position. The dotted lines indicate
minimal variation in the position of various features
of the spectra. This suggests that the oxygen stoi-
chiometry remains consistent throughout the oxide
region. Scale bars represent 10 nm.
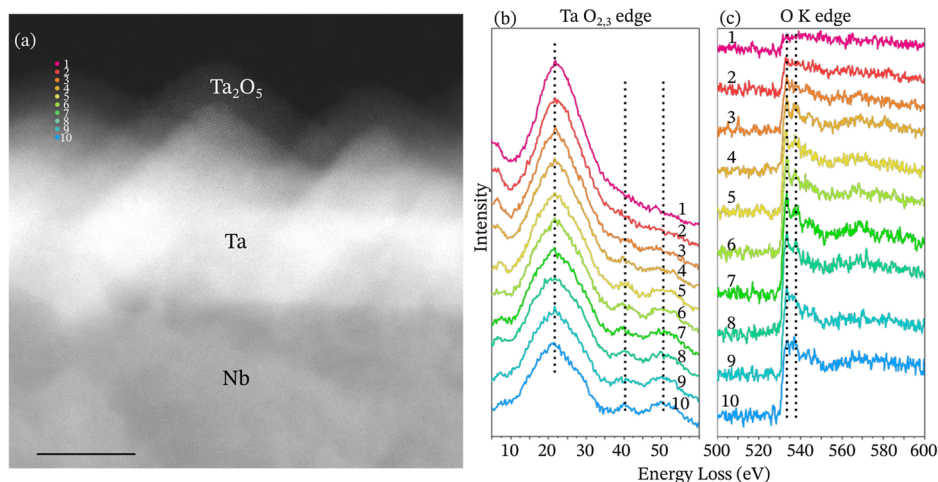
the surface of the TiN-capped Nb qubit is found to be the thinnest oxide whereas the 5–7 nm Ta_2O_5 observed at the surface of the Ta-capped Nb qubit prepared on silicon is found to be the thickest.

Therefore, our findings help explain why previous experimental studies with qubits prepared from Ta metal exhibited improved T_1 values[13,14]. Namely, our results suggest the improved T_1 predominantly arises from the presence of a less lossy surface oxide, as opposed to the tantalum film being less lossy compared to niobium films.

To understand the difference in performance between the capped and baseline samples, we use electron microscopy and, in particular, electron energy loss spectroscopy (EELS) to further evaluate the chemical nature of the Ta oxide. EELS signals captured from points 1-10 on the dark field image of the Ta_2O_5/Ta interface of the prepared qubit are provided in Fig. 6. From this image, we observe that the oxide thickness of Ta is roughly similar to that observed for Nb oxide (4–5 nm). The Ta oxide is found to be predominantly amorphous based on the presence of diffuse diffraction patterns taken in this region (Fig. S4). Features associated with the tantalum $O_{2,3}$ edge are labeled with a dotted line in Fig. 6b and those associated with the oxygen K edge are labeled with a dotted line in Fig. 6c. We find there are changes in the shape of both set of features, but the position of oxygen K edge remains constant. This indicates that the Ta predominately exists in a 5+ state. This is in contrast to what has been observed in Nb. For Nb, shifts in the features accompanying the onset of the oxygen K edge are observed as a function of position in the oxide due to spatial variations in the valence state[37,38]. This suggests that the Ta oxide present in these capped samples is largely free of sub-stoichiometric regions.

Finally, the X-ray reflectivity signal captured from both the Nb sample as well as the Ta-capped Nb sample is provided in Fig. S5. Based on the data fits performed using dynamical scattering theory[39], we observe that the surface oxide of Nb consists of roughly 4.1 nm of Nb_2O_5 and 0.5 nm of NbO whereas the surface oxide of Ta consists entirely of 5.9 nm of Ta_2O_5. This technique suggests that the capped samples are largely free of sub-oxides and is consistent with the TEM findings.

Theoretical and experimental findings have linked the variable oxygen content in the Nb oxide layer to the presence of local paramagnetic moments. These moments are a source of flux noise, dephasing, and energy loss[40,41]. We hypothesize that the stoichiometric, predominantly Ta_2O_5 layer of Ta-capped Nb reduces the potential for moment formation compared to the variable oxygen content observed in the Nb oxide layer of uncapped Nb. Additionally, it is possible the Ta oxide layer hosts fewer TLS in the frequency range of the qubit frequency compared to the Nb oxide layer. This is an area of continuing active exploration through experimental and theoretical studies. In summary, we have implemented different passivation strategies to eliminate and prevent the formation of lossy Nb surface oxides in Nb superconducting qubits. By capping Nb films with Ta, Al, TiN, and Au, we are able to systematically improve the average qubit relaxation times. Of these capping strategies, we find that Nb films capped with Ta and Nb films capped with Au yield the highest median T_1. We observe similar improvements in median T_1 when superconducting qubits are prepared on silicon as well as sapphire. Together, this methodology offers a solution to delivering state-of-the-art devices with median T_1 times exceeding 300 μs that is compatible with industrial-level processes. Further, this method offers a pathway for continuing to suppress the dielectric loss associated with the metal/air interface through further exploration of capping Nb film with ambient-stable layers prior to air exposure and is applicable to the field of superconducting devices broadly (quantum information science, detectors for cosmic science, and particle accelerators). Finally, this study provides strong indication that the Nb oxide is more lossy than the tantalum oxide and will help guide future investigations aimed at building a microscopic understanding of TLS sources in superconducting qubits.

Disclaimer

Certain commercial equipment, instruments, or materials are identified in this paper in order to specify the experimental procedure adequately. Such identification is not intended to imply recommendation or endorsement by NIST, nor is it intended to imply that the materials or equipment identified are necessarily the best available for the purpose.

Data availability

The data that support the findings of this study are available from the corresponding author upon reasonable request.

References

1. Kjaergaard, M. et al. Superconducting qubits: current state of play. *Annu. Rev. Condens. Matter Phys.* **11**, 369–395 (2020).
2. Wendin, G. Quantum information processing with superconducting circuits: a review. *Rep. Prog. Phys.* **80**, 106001 (2017).
3. de Leon, N. P. et al. Materials challenges and opportunities for quantum computing hardware. *Science* **372**, eabb2823 (2021).
4. Burnett, J. J. et al. Decoherence benchmarking of superconducting qubits. *npj Quantum Inf.* **5**, 54 (2019).
5. Schlör, S. et al. Correlating decoherence in transmon qubits: low frequency noise by single fluctuators. *Phys. Rev. Lett.* **123**, 190502 (2019).

6. Nersisyan, A. et al. Manufacturing low-dissipation superconducting quantum processors. (2019).

7. Wilen, C. D. et al. Correlated charge noise and relaxation errors in superconducting qubits. *Nature* **594**, 369–373 (2021).

8. Simmonds, R. W. et al. Decoherence in Josephson phase qubits from junction resonators. *Phys. Rev. Lett*. **93**, 077003 (2004).

9. Müller, C., Cole, J. H. & Lisenfeld, J. Towards understanding two-level-systems in amorphous solids: insights from quantum circuits. *Rep. Prog. Phys.* **82**, 124501 (2019).

10. McDermott, R. Materials origins of decoherence in superconducting qubits. *IEEE Trans. Appl. Supercond.* **19**, 2–13 (2009).

11. Tolpygo, S. K. et al. Fabrication process and properties of fully-planarized deep-submicron Nb/Al– AlO_x/Nb Josephson junctions for VLSI circuits. *IEEE Trans. Appl. Supercond*. **25**, 1–12 (2015).

12. Romanenko, A. et al. Three-dimensional superconducting resonators at 20 mK with photon lifetimes up to $\tau = 2$ s. *Phys. Rev. Appl.* **13**, 034032 (2020).

13. Place, A. P. M. et al. New material platform for superconducting transmon qubits with coherence times exceeding 0.3 milliseconds. *Nat. Commun.* **12**, 1779 (2021).

14. Wang, C. et al. Towards practical quantum computers: transmon qubit with a lifetime approaching 0.5 milliseconds. *npj Quantum Inf.* **8**, 3 (2022).

15. Romanenko, A. & Schuster, D. I. Understanding quality factor degradation in superconducting niobium cavities at low microwave field amplitudes. *Phys. Rev. Lett.* **119**, 264801 (2017).

16. Murthy, A. A. et al. Developing a chemical and structural understanding of the surface oxide in a niobium superconducting qubit. *ACS Nano* **16**, 17257–17262 (2022).

17. Niepce, D., Burnett, J. J., Latorre, M. G. & Bylander, J. Geometric scaling of two-level-system loss in superconducting resonators. *Supercond. Sci. Technol.* **33**, 025013 (2020).

18. Bafia, D., Grassellino, A. & Romanenko, A. Probing the role of low-temperature vacuum baking on photon lifetimes in superconducting niobium 3-d resonators. Preprint at http://arXiv.org/abs/2108.13352 (2021).

19. Burnett, J., Faoro, L. & Lindström, T. Analysis of high-quality superconducting resonators: consequences for TLS properties in amorphous oxides. *Supercond. Sci. Technol.* **29**, 044008 (2016).

20. Premkumar, A. et al. Microscopic relaxation channels in materials for superconducting qubits. *Commun. Mater.* **2**, 72 (2021).

21. McRae, C. R. H. et al. Materials loss measurements using superconducting microwave resonators. *Rev. Sci. Instrum.* **91**, 091101 (2020).

22. Checchin, M., Frolov, D., Lunin, A., Grassellino, A. & Romanenko, A. Measurement of the low-temperature loss tangent of high-resistivity silicon using a high-Q superconducting resonator. *Phys. Rev. Appl*. **18**, 034013 (2022).

23. Verjauw, J. et al. Investigation of microwave loss induced by oxide regrowth in high-Q niobium resonators. *Phys. Rev. Appl*. **16**, 014018 (2021).

24. Altoé, M. V. P. et al. Localization and mitigation of loss in niobium superconducting circuits. *PRX Quantum* **3**, 020312 (2022).

25. Knobloch, J. The "Q disease" in superconducting niobium rf cavities. *AIP Conf. Proc*. **671**, 133–150 (2003).

26. Romanenko, A., Barkov, F., Cooley, L. D. & Grassellino, A. Proximity breakdown of hydrides in superconducting niobium cavities. *Supercond. Sci. Technol.* **26**, 035003 (2013).

27. Lee, J. et al. Discovery of Nb hydride precipitates in superconducting qubits. Preprint at http://arXiv.org/abs/2108.10385 (2021).

28. Zheng, K. et al. Nitrogen plasma passivated niobium resonators for superconducting quantum circuits. *Appl. Phys. Lett*. **120** (2022). https://doi.org/10.1063/5.0082755. 102601.

29. Fang, X. et al. Understanding mechanism of performance improvement in nitrogen-doped niobium superconducting radio frequency cavity. *Mater. Res. Lett.* **11**, 108–116 (2023).

30. Murthy, A. A. et al. ToF-SIMS analysis of decoherence sources in superconducting qubits. *Appl. Phys. Lett*. **120**, 044002 (2022).

31. Lu, X. et al. Stability, metallicity, and magnetism in niobium silicide nanofilms. *Phys. Rev. Mater.* **6**, 064402 (2022).

32. Clerk, A. A. & Utami, D. W. Using a qubit to measure photon-number statistics of a driven thermal oscillator. *Phys. Rev. A* **75**, 042302 (2007).

33. Vaaranta, A., Cattaneo, M. & Lake, R. E. Dynamics of a dispersively coupled transmon qubit in the presence of a noise source embedded in the control line. *Phys. Rev. A* **106**, 042605 (2022).

34. Krantz, P. et al. A quantum engineer's guide to superconducting qubits. *Appl. Phys. Rev.* **6**, 021318 (2019).

35. Klimov, P. et al. Fluctuations of energy-relaxation times in superconducting qubits. *Phys. Rev. Lett.* **121**, 090502 (2018).

36. You, X. et al. Stabilizing and improving qubit coherence by engineering the noise spectrum of two-level systems. *Phys. Rev. Appl.* **18**, 044026 (2022).

37. Tao, R. et al. Electron energy-loss spectroscopy study of metallic Nb and Nb oxides. *J. Appl. Phys*. **110**, 124313 (2011).

38. Oh, J.-S. et al. In-Situ Transmission Electron Microscopy Investigation on Surface Oxides Thermal Stability of Niobium. *Appl. Surf. Sci.* **627**, 157297 (2023).

39. Nelson, A. Co-refinement of multiple-contrast neutron/x-ray reflectivity data using motofit. *J. Appl. Crystallogr.* **39**, 273–276 (2006).

40. Sheridan, E. et al. Microscopic theory of magnetic disorder-induced decoherence in superconducting Nb films. Preprint at http://arXiv.org/abs/2111.11684 (2022).

41. Proslier, T., Kharitonov, M., Pellin, M. & Zasadzinski, J. Evidence of surface paramagnetism in niobium and consequences for the superconducting cavity surface impedance. *IEEE Trans. Appl. Supercond.* **21**, 2619–2622 (2011).

Acknowledgements

Author contributions

M.B., A.M., S.Z., and F.C. contributed equally to this manuscript. The project was conceived by M.B., A.M., S.Z., F.C., A.R., and A.G. The devices are fabricated by M.B., F.C., I.N., H.C., J.M., K.V. The measurements were performed by A.M., S.Z., E.L., D.M., J.L., J.O., L.Z., D.G., C.G., M.B., and M.H. The experimental data was analyzed by M.B., A.M., S.Z., F.C., X.Y., Z.H., T.R., J.L., D.v.Z., R.P., I.N., A.L., D.B., Y.K., C.K., E.L., D.M., J.M., M.R., H.C., J.M., D.P., K.V., K.Y., J.S., L.Z., M.K., F.Q., D.G., C.T., G.P., V.D., J.R., M.B., M.H., J.Z., J.K., J.S., A.R., and A.G. A.M. wrote the manuscript together with M.B., S.Z., F.C., A.R., and A.G. All authors discussed the results and the manuscript.

Competing interests

All authors declare no competing interests.

Additional information

Supplementary information The online version contains supplementary material available at https://doi.org/10.1038/s41534-024-00840-x.

Correspondence and requests for materials should be addressed to Alexander Romanenko or Anna Grassellino.

Reprints and permissions information is available at http://www.nature.com/reprints

Publisher's note Springer Nature remains neutral with regard to jurisdictional claims in published maps and institutional affiliations.